d-^{3}He REACTION MEASUREMENTS DURING FAST WAVE MINORITY HEATING IN PLT

R. E. Chrien*, J. D. Strachan

Plasma Physics Laboratory, Princeton University, Princeton, New Jersey 08540

Time- and energy- resolved d-^{3}He fusion reactions have been measured to infer the energy of the d^+ or He^{++} minority ions heated near their cyclotron frequency by the magnetosonic fast wave. The average energy of the reacting ^{3}He ions during ^{3}He minority heating is in the range of 100-400 keV, as deduced from the magnitude of the reaction rate, its decay time, and the energy spread of the proton reaction products. The observed reaction rate and its scaling with wave power and electron density and temperature are in qualitative agreement with a radial reaction rate model using the minority distribution predicted from quasilinear velocity space diffusion. Oscillations in the reaction rate are observed concurrent with sawtooth and m=2 MHD activity in the plasma.

*Present Address: Los Alamos National Laboratory, Los Alamos, New Mexico 87540

I. INTRODUCTION

Ion Cyclotron Range-of-Frequency (ICRF) heating is an attractive auxiliary heating method in tokamak experiments.[1-9] ICRF heating experiments employ the fast magnetosonic wave in either the mode conversion or minority regimes. In the mode conversion regime, the fast wave is converted to the slow Ion Bernstein wave near the two-ion hybrid layer of a two-ion species plasma which then heats the resonant ions (cyclotron damping) or the electrons (Landau damping). If one of the ion species is sufficiently dilute and hot, the fast wave can damp predominately on it directly (minority regime) and produce a non-Maxwellian minority distribution which heats the majority ions and electrons through Coulomb collisions. ICRF heating experiments in small, low plasma current tokamaks have demonstrated effective heating in the mode conversion regime,[7] whereas the minority regime in some cases has been complicated by increased impurity radiation and density rise,[7] presumably due to unconfined energetic minority ions striking the wall.[10] However, the minority heating experiments in the Princeton Large Torus (PLT), which has good energetic ion confinement, have produced efficient ion heating[5] and large fusion reactivity[11] due to the energetic minority component.

This paper reports time- and energy- resolved measurements of $d(^3He,p)^4He$ fusion reactions in PLT during ICRF minority heating of either $^3He^{++}$ or d^+ in a majority plasma of the other species. Information about the energy distribution of the minority species is obtained by measurements of the spectrum, magnitude, and time evolution of the escaping 14.7 MeV $d-^3He$ protons, which are detected with silicon surface barrier detectors. The scalings of the reaction rate with ICRF power, electron density, and temperature are in qualitative agreement with a reaction rate model based on the minority distribution predicted from

quasilinear RF diffusion. The d-^{3}He reaction rate can exhibit oscillations which are related to the sawtooth or m=2 oscillations in the tokamak discharge.

II. THEORY

For fast wave minority heating the two-ion hybrid layer, which is located between the cyclotron resonance layers of the two-ion species, influences the minority heating by increasing the left-handed component of the fast waves.[13] The minority heating is also enhanced by the presence of a non-Maxwellian minority distribution.[4,14] For the case of waves launched from the low magnetic field side of a tokamak plasma with a large charge-to-mass ratio minority compared to the majority, numerical calculations[13] of the wave propagation and damping showed that the wave power is absorbed primarily by the minority ions, even for appreciable minority concentrations (20%). In contrast, for the case of a smaller e/m minority species, the minority power absorption decreases strongly with increasing concentration due to the shielding effect of the two-ion layer which in this case is encountered before the minority cyclotron layer. The calculations also predict that the radial power deposition to the minority ions is centrally peaked with virtually no surface heating.

The production of energetic non-Maxwellian minority ion distributions is the subject of a theory of Stix.[14] He includes a quasilinear-type RF diffusion coefficient[15] with the Fokker-Planck terms in the Boltzmann equation to describe diffusion in velocity space for resonant ions crossing the cyclotron layer. When the phase velocity of the wave is much larger than the ion thermal velocity, the diffusion is primarily in $v_\perp$. Pitch angle scattering serves to keep the distribution nearly isotropic at low energies. At higher energy, pitch angle scattering becomes less important than electron drag so the distribution

becomes strongly anisotropic ($v_\perp >> v_\parallel$). Stix presents explicit expressions for the distribution in these two limits. In both cases, the tail temperature of the minority distribution is determined by the product of the wave power per minority ion and the ion slowing down time due to electron drag. The tail temperature for the anisotropic limit is increased by 50% since the wave power is not shared with the parallel degree of freedom. The transition between the isotropic and $v_\perp >> v_\parallel$ solutions is approximately at the energy where the rates of pitch angle scattering and electron drag are equal (approximately 100 keV for PLT). The $v_\perp >> v_\parallel$ solution is derived with the assumption that $k_\perp \rho_{min}$ is small, where $k_\perp$ is the wave number perpendicular to the magnetic field and ρ_{min} is the minority gyroradius, which is invalid for the high minority energies in PLT. The approximation overestimates the power deposited in the tail of the minority distribution and hence the number of fusion reactions.

We have developed a one-dimensional model to calculate the d-^{3}He reaction rate during ICRF minority heating experiments. We divide the plasma into radial shells and in each shell calculate the minority ion distribution predicted by Stix. We use the isotropic solution f_{is} below E_{trans} (Figure 1), where $E_{trans} = 22.2\ T_e\ (2\ A^{1/2}\ Z_{eff})^{2/3}$ is the energy at which the $v_\perp >> v_\parallel$ solution is expected to become valid.[14] Here, A is the atomic mass of the minority ions, T_e is the electron temperature in keV, and $Z_{eff} = \sum n_i Z_i^2 / n_e$ is the effective impurity number of the plasma. Above E_{trans}, we integrate the product of $f_\parallel = f_{is}(E_\parallel < E_{trans})$ and $f_\perp = f_{anis}(E_\perp)$ over the allowed velocity space pitch angles, where f_{anis} is the $v_\perp >> v_\parallel$ solution. The distributions are calculated using a gaussian power deposition profile with a characteristic width σ (power density $\propto \exp(-r^2/2\sigma^2)$) and density and temperature profiles proportional to $(1-(r/a)^2)^x$ where typically x=1 (x=2) for the density (temperature) profiles.

The d-^{3}He fusion reactivity is calculated from the minority ion distribution:

$$\langle\sigma v\rangle = \int \sigma(v)\ v\ f(v)\ d^3v \ / \int f(v)\ d^3v$$

$$= (2/m)^{1/2} \int f(E)\ \sigma(E)\ E\ dE \ / \int f(E)\ E^{1/2} dE.$$

Duane's fit[16] is used for the d-^{3}He fusion cross section. When calculating the reactivity of a ^{3}He minority distribution, the cross section is evaluated as $\sigma(E/1.5)$ to obtain the correct relative velocity. We are concerned with cases in which the energy of the minority ions is very large, so we neglect thermal corrections due to the majority ions in calculating the reactivity. The reactivity for the distribution in Figure 1 is shown as a function of the upper energy cutoff of the reactivity integral. The reactivity integral must be cut off at the energy at which the minority ions become unconfined. The energy cutoff is always in the anisotropic part of the minority ion distribution for typical plasma currents (> 200 kA) in PLT. The first unconfined orbit in this case is a banana orbit which touches the outer limiter. It is one of the continuous orbit solutions[17] which is calculated by conservation of energy, magnetic moment, and canonical angular momentum between the initial position and the limiter position. The reactivity calculation is averaged over the radial shell to account for differing cutoff energies at different poloidal angles. The energy cutoff is more important for a d^+ minority than a $^3He^{++}$ minority since the lost energy is about 2.5 times lower for d^+.

The d-^{3}He reaction rate is calculated for 1 cm radial shells. The total d-^{3}He reaction rate is obtained by summing the reaction rates per shell. The predicted d-^{3}He reaction rate is very sensitive to the electron temperature and density, the minority density, and the power deposition profile width. Of these quantities, the last two are not well-known experimentally. However, the

reaction rate is expected to be peaked near the center due to the peaking of the power deposition and temperature profiles.

III. DETECTOR SYSTEMS AND CALIBRATION

Time-integrated activation sample measurements of d-^{3}He reactions during minority heating have previously been reported.[11] In this work we have used two silicon surface barrier detector systems to make time- and energy- resolved measurements of the d-^{3}He protons.

Time-resolved d-^{3}He measurements were performed with a probe- mounted surface barrier detector (proton probe) located on the horizontal midplane of the torus. The detector was 160° toroidally displaced from the limiter and mounted on a port aligned 42° from perpendicular to the vacuum vessel. The detector was positioned 0.5 to 2.5 cm inside the vessel and about 9 cm from the plasma.

The silicon surface barrier detector had an active area of 0.3 cm × 2.3 cm. An applied reverse bias (typically 50 V) created a 300 μm depleted depth. Electron-hole pairs were created by each 3.6 eV of proton energy deposited in the detector, resulting in a current pulse proportional to the total energy deposited.

Protons incident on the detector from above passed through a collimating slit in a 0.3 cm thick stainless steel cap surrounding the detector holder [Figure 2(a)]. The slit was covered with a 75 μm stainless steel foil to shield against electrical noise, other fusion products, and plasma particles. The protons then passed through a second slit and 255 μm foil in the detector

holder. They lost about 6.5 MeV of energy in the foils and deposited about 3 MeV in the depleted region of the detector.

The proton probe was affected by three types of interference in PLT operation. The detector was sensitive to hard X rays which penetrated the stainless steel cap. This limited the use of the probe to locations away from the limiter and to discharges in which the runaway electron levels were low. Second, the probe was sensitive to vibration from the tokamak pulse, which made it necessary to support rigidly the detector holder and coaxial line within the probe housing. Finally, the detector was apparently affected by heat. At times when the detector was too close to the plasma, its leakage current increased indicating that its resistance had dropped. It was necessary to ensure that the probe was not inserted too far or that the plasma did not ride out in major radius.

The current pulses from the detector were measured by a low-noise, charge-sensitive preamplifier. The amplifier output was connected to a pulse height analyzer and to a single channel analyzer (SCA) and scaler which provided pulse counting with 10 ms time resolution. The SCA discriminator was set above the noise level from hard X rays and vibration. Before installation on PLT, the energy calibration was established with a ^{228}TH alpha source which has six peaks between 5 and 9 MeV. The calibration procedure included the alpha energy loss in passing through 0.1 cm of air and the 50 $\mu g/cm^2$ aluminum front surface of the detector.

The proton detection efficiency of the detector was established during deuterium neutral beam injection into a deuterium plasma containing a small concentration of ^{3}He.[18] The detector efficiency was determined by the linear relatiohship observed between the number of detector counts and the number of d-^{3}He reactions expected for beam-target fusion production. The number of d-^{3}He

reactions expected was calculated using a bounce-averaged Fokker-Planck code for the beam ions.[19] The ^3He density used as input for this code was measured from the electron density rise associated with ^3He gas puffing during ohmically heated discharges. This method is uncertain because of residual ^3He remaining from previous discharges and because of the effects of the neutral beam heating on gas influx. Another uncertainty is the deuterium density which can be less than $(n_e - 2n_{^3He})$ due to impurities in the plasma. The detector efficiency obtained by this method was 1.5×10^{-6} protons/d-^3He reaction with an uncertainty of about a factor of three.

The detection efficiency of the proton probe was also calculated by following the particle orbits from the detector back into the plasma. If we follow a differential solid angle, $d\Omega$, from the detector for a path length, ℓ, into the plasma, then the area subtended is $f\ell^2 d\Omega$ where the factor $f<1$ ($f>1$) accounts for any possible focusing (defocusing) by the magnetic field. The reaction rate for an element of path length $d\ell$ is $f\, S(r)\ell^2 d\ell\, d\Omega$ where $S(r)$ is the reaction rate per unit volume. The volume element produces a flux per reaction at the detector of $(4\pi f\ell^2)^{-1}$ where the effect of focusing is inverted; that is, it increases the flux at the detector. The differential count rate is then $S(r)\, A \cos\theta\, d\ell\, d\Omega$ where A is the detector area and θ is the angle of the proton from the detector normal. The detector efficiency ε is then

$$\varepsilon = (A/4\pi) \int S(r)\cos\theta\, d\ell\, d\Omega \,/\, \int S(r) d^3r.$$

The largest contribution to the detector efficiency was due to protons with $\theta \simeq 0$. Those orbits saw the largest effective detector area. They also had the largest gyro-radii and therefore the closest approach to the plasma center (where $S(r)$ was largest) from the detector location. The solid angle of the detector was partially reduced by its proximity to the vessel wall.

The efficiency was evaluated numerically by integrating along the actual proton orbits backward from the detector and integrating over the solid angle defined by the collimating slits. For comparison with the experimental calibration we used the S(r) calculated for beam-target reactions.[18] We found that the calculated efficiency was 9×10^{-7}, which agrees with the experimental calibration (1.5×10^{-6}) within the uncertainty in the measurement. The calculated efficiency itself has an uncertainty of about a factor of two due to its sensitivity to the width of S(r), which is not experimentally known for ICRF heating, since protons born near the plasma center can barely reach the probe location. The effect of an outward Shafranov shift of the plasma center was small for the beam-target S(r). An outward shift of 10 cm caused the calculated efficiency to increase by 14%; a 15 cm shift caused a 9% increase over the centered case. The reaction rate measurements reported in this paper were obtained using the experimentally determined efficiency.

The differential detector efficiency per unit path length $d\varepsilon/d\ell$ as a function of minor radius is shown in Figure 3(a). The proton orbits cause $d\varepsilon/d\ell$ to be peaked near the center of the plasma.

The pulse counting method used with the proton probe could operate up to a count rate of $\simeq 5 \times 10^4$ s^{-1} which represented a maximum d-^{3}He reaction rate of about 3×10^{10} s^{-1}. In order to measure higher reaction rates, we used a charge-sensitive amplifier to measure the detector current. The amplifier bandwidth was 1 MHz. The frequency response of the complete system was tested up to 100 kHz with a light-emitting diode. The amplifier output V_{out} for a given d-^{3}He reaction rate R_{d-^3He} was calculated from the amplifier gain, the detector efficiency, the energy deposited per proton, and the charge created per unit energy.

Measurements of the d-^{3}He proton energy spectrum were performed with a silicon surface barrier detector located at the bottom of the PLT vessel (proton spectrometer). Protons entered the spectrometer [Figure 2(b)] with approximately zero parallel velocity and 40° elevation through five 0.17 cm diameter collimating holes. The detector had a depleted region of 1000 μm for an applied bias of 350 V. The entrance angle of 40° was chosen to increase the proton path length in the detector so that protons with energy up to 15.5 MeV would deposit their full energy in the depleted region. It also ensured that the detector did not have a line-of-sight view of plasma within the limiter radius. Damage to the top surface of the detector was prevented by the use of a 12.7 μm beryllium foil at the detector surface.

The finite width of the collimating holes permitted the incident protons to have a range of angles to detector suface. Curvature of the orbits due to the proton gyromotion decreased the angle of elevation. We calculated that the protons could have angles between 44° and 29° corresponding to complete proton energy deposition in the detector of between 14.8 MeV and 18 MeV. The presence of the beryllium foil caused the protons to lose between 90 keV and 130 keV for the range of possible angles with a statistical variation of about 50%. The energy loss and detector response were calculated using analytic fits to the data for proton energy loss in beryllium and silicon.[20]

The resolution of the spectrometer was influenced by several effects. The beryllium foil contributed an energy spread of about 100 keV. The capacitance of the detector (7.5 pF) and the coaxial line to the preamplifier (60 pF) caused a noise width of only 5 keV. Vibration of the detector during a discharge could introduce additional noise. The effect of vibration was measured by introducing a precision pulser signal into the preamplifier with the detector connected. From the width of the pulser line, we found that vibration typically introduced

about 120 keV of noise. The detector resolution, calculated from the root mean square of these effects, was 160 keV.

The detection efficiency of the proton spectrometer was calculated using the orbit code. The efficiency was 4.4×10^{-8} for 27 kG magnetic field. Increasing the magnetic field to 32 kG raised the efficiency to 5.9×10^{-8} since the proton orbits were closer to the plasma center and took longer to drift to the detector. A 10 cm outward major radial shift of the plasma center caused a small (3%) decrease in the efficiency; a 15 cm shift reduced the efficiency by 12%. The differential detector efficiency $d\varepsilon/d\ell$ as a function of minor radius [Figure 3(b)] was broader than for the proton probe. In this case, the proton gyro-orbit averaged over the central 20 cm of the plasma while drifting downward to the detector.

The relative efficiency of the proton spectrometer and proton probe measured during ICRF ^{3}He minority heating was found to be 0.083. Using the measured efficiency of the proton probe, this implied that the spectrometer efficiency was 1.2×10^{-7}. This is three times higher than the calculated efficiency, which is within the estimated uncertainty.

IV. d-^{3}He PROTON SPECTRA

The d-^{3}He proton spectrum was measured both during deuterium neutral beam injection and during ^{3}He minority ICRF heating. The velocity distribution of the energetic ions was well-known from charge exchange measurements for neutral beam injection. Charge exchange measurements during ^{3}He minority heating have not been successfully performed due to the low probability of the double charge exchange process.

Measurements of the d-^{3}He proton spectrum during deuterium neutral beam injection into a deuterium plasma containing a small concentration of ^{3}He were performed in PLT (major radius = 132 cm, minor radius = 40 cm, toroidal field $\leq$ 32 kG, plasma current $\leq$ 500 kA) using two 40 keV beams injected parallel to the plasma current (co-injection) with about 1 MW of power. The electron and ^{3}He line-averaged densities were about 2.5 x 10^{13} cm^{-3} and 2 x 10^{12} cm^{-3}, respectively.

The spectrum measured with the proton spectrometer (Figure 4) showed a peak centered at 14.6 MeV with FWHM of 0.64 MeV. The spectrum was consistent with a proton spectrum centered at 14.7 MeV. The spectrum showed some counts up to 17.5 MeV. We believe that these were due to pileup of the 14.7 MeV proton counts with 3.0 M protons from the d(d,p)t fusion reaction that are also detected by the spectrometer. The d-d reaction rate is about 10^2 times larger than the d-^{3}He rate under these conditions.[1]

Calculations of the beam product spectrum during neutral beam injection have been performed for collimated detectors.[21] For the case of protons produced with 90° pitch angle (matching the detector acceptance) and Z_{eff} = 3, the FWHM of the proton spectrum is 0.43 MeV (Figure 4), which is 50% smaller than the measured proton spectrum. The PLT neutral beams produce electrical noise associated with their ion sources that is seen as a broadening of the pulser signal connected to the preamplifier. The width of the proton spectrum in Figure 10 may have been broadened either by pileup with d-d protons or by the neutral beam electrical noise.

The d-^{3}He proton spectrum was also measured during ^{3}He minority ICRF heating. Unlike the neutral beam measurement, the neutron emission was low ($\leq$ 2 x 10^{12} s^{-1}) so there was no interference due to pileup with d-d proton

counts. The noise width of the pulser signal was 120 keV. The spectrum was measured during 350 kW ICRF heating at 24.6 MHz.

The measured spectra for plasma currents of 500 kA and 250 kA are shown in Figure 5. The electron density was 2.5×10^{13} cm^{-3} and 2.0×10^{13} cm^{-3} for the two cases. The spectra had FWHM of 2.3 MeV and 2.0 MeV, respectively. The spectra were wider than the neutral beam case, reflecting the high energy of the ^{3}He tail produced by ICRF minority heating. The spectral shape was asymmetric, showing a downward shift in energy with the peak at about 14.0 MeV. The shift was possibly due to a broad proton spectrum with a significant number of protons which did not deposit their full energy in the detector.

The proton spectrum was used to estimate the energy of the ^{3}He ions responsible for the reactions. Using non-relativistic reaction kinematics, the proton energy for the reaction $d(^3He,p)\alpha$ is approximately

$$E_p = 14.7 \text{ MeV } (1 + \cos\theta((3/5)\ E_{^3He}/(18.3 \text{ MeV}))^{1/2}) .$$

Both the energetic ^{3}He ions and the protons reaching the spectrometer were expected to be nearly perpendicular to the magnetic field. The upper and lower energy limits of the spectrum then corresponded to $\cos\theta = \pm 1$. The ^{3}He energy in terms of the width of the spectrum ΔE_p is

$$E_{^3He} = (5/3)(18.3 \text{ MeV})((\Delta E_p/2)/14.7 \text{ MeV})^2 .$$

Using this estimate, we found that the ^{3}He energy was about 190 keV for the 500 kA case and 140 keV for the 250 kA case. These estimates are conservative since we have used the FWHM for ΔE_p. Near the plasma center these ^{3}He energies are confined in PLT for both cases. They were consistent with the tail temperature expected for the conditions in this experiment (T_{eff} = 50 keV), assuming that the central power and ^{3}He densities were about 0.6 W/cm^3 and 2×10^{12} cm^{-3}, respectively. The lower energy estimated for the 250 kA case was consistent with about 25% lower electron temperature.

V. d-^{3}He REACTION RATE

A. ^{3}He MINORITY HEATING

Most of the d-^{3}He data was obtained during fundamental ^{3}He minority heating in a deuterium majority plasma. This heating mode has proven to be highly efficient, yielding a deuterium heating rate of 4-6 eV × 10^{13} cm^{-3} kW^{-1} in experiments with up to 1 MW coupled to the plasma.[5] We found that the ion heating and d-^{3}He reaction rate were optimized under the same plasma conditions for a given density, but the d-^{3}He rate was more sensitive to small changes in plasma conditions.

The d-^{3}He rate was observed to depend strongly on the power per particle and collisional drag which theoretically determine the effective temperature T_{eff} of the ^{3}He tail. The wave power per ^{3}He ion was determined by the total wave power, the power deposition profile, and the ^{3}He density. The ^{3}He slowing down time was determined by the electron density and temperature, $\propto T_e^{3/2}/n_e$. For typical profiles, the slowing down time was longest in the plasma center so the d-^{3}He rate should have been largest when the power deposition was centrally peaked. Evidence for central power deposition was obtained from an experiment in which the cyclotron layer was varied in major radius; the best ion heating and d-^{3}He rates were obtained when the cyclotron layer was positioned near the plasma center.[11]

The d-^{3}He rate increased strongly with ICRF power P_{RF} [Figure 6(b)], varying as $P_{RF}^{2\to3.5}$. At the highest power levels, strong sawtooth oscillations were usually present on the proton signal; here we have plotted the maximum d-^{3}He rate before the sawtooth drop. The d-^{3}He rate showed no evidence of saturation up to the maximum power in this experiment.

The d-^{3}He rate decreased with electron density [Figure 6(a)], proportional to n_e^{-3}. This density scaling tended to limit the maximum d-^{3}He rate due to the density rise associated with large ICRF powers. When the power scan data are corrected for density rise, the combined scaling of d-^{3}He rate obtained from Figure 6 is $P_{RF}^{3.4} n_e^{-3}$.

The d-^{3}He rate tended to increase with electron temperature. In one experiment, the electron temperature was increased by using 900 kW of hydrogen neutral beam injection. Thomson scattering measurements showed a central electron temperature of T_e = 1.5 keV during 600 kW ICRF heating alone and T_e = 1.8 keV during combined ICRF and neutral beam heating. The d-^{3}He rates at various densities for this comparison are shown in Figure 7. The electron temperature difference was smaller for the low density points where the neutral beam electron heating was less effective.

We assessed the influence of plasma current on d-^{3}He rate by scanning in ICRF power at full (480 kA) and 70% (340 kA) currents (Figure 6). In both cases the d-^{3}He rate was proportional to $P_{RF}^{2+3.5}$ with no evidence of saturation up to the highest power available. The d-^{3}He rate was lower at the same power for the 70% current case, possibly due to lower electron temperature (not measured).

The ^{3}He density had a qualitative effect on the d-^{3}He reaction rate. The d-^{3}He rate dropped as much as 50% when the ^{3}He density was increased over its optimum setting. If the ^{3}He density was decreased, the ICRF coupling to the plasma exhibited peaks in the loading resistance characteristic of discrete toroidal eigenmodes; the d-^{3}He rate did not further increase under these conditions. The optimum ^{3}He density was in the range of 5% to 10%, as measured by the electron density rise from the ^{3}He gas puff during ohmic heating.

The d-^{3}He rate could be substantially increased by deuterium neutral beam injection, probably due to reactions between the 40 keV injected deuterons and the energetic ^{3}He tail. In one experiment, 1.3 MW of ICRF power was combined with 0.6 MW deuterium co-injection. The d-^{3}He rate was 1.6×10^{14} s^{-1} at $\bar{n}_e = 4 \times 10^{13}$ cm^{-3}, while the ICRF heating alone produced a d-^{3}He rate of 1.1×10^{14} s^{-1} at $\bar{n}_e = 3.2 \times 10^{13}$ cm^{-3}. Using the observed n_e scaling, we find that deuterium injection provided an enhancement factor of 2.8 in the reaction rate when normalized to constant density.

MHD activity in the discharge had a significant effect on the d-^{3}He rate. The largest rates were obtained in the presence of strong sawtooth activity in the central soft x-ray emission. In contrast, m=2 activity seemed to be detrimental to the reaction rate. During a run in which sawtooth and m=2 activity alternated from shot to shot, the d-^{3}He rate was as much as 60% lower during m=2 discharges despite 30% lower density. The electron temperature was also lower during the m=2 discharges (1.1 keV vs. 1.5 keV for sawtooth discharges).

B. d^+ MINORITY HEATING

d-^{3}He rates were also measured during fundamental d^+ minority heating in a predominantly ^{3}He plasma. Direct d^+ minority heating is possible only for very dilute (<5%) d^+ concentrations due to the screening effect of the two-ion hybrid layer.[13]

We obtained a partial toroidal field B_T scan (up to the maximum PLT field of 32 kG) at 680 kW of ICRF power [Figure 8(a)]. The d-^{3}He rate was largest for cyclotron layer positions near the plasma center, similar to the ^{3}He minority B_T

scan. The d-d reaction rate produced by the d^+ minority showed similar behavior.

The d-^{3}He rate increased with ICRF power P_{RF} up to 665 kW [Figure 8(b)], proportional to $P_{RF}^{4.5}$. The d-d rate also increased approximately as $P_{RF}^{3.7}$. There was no saturation of reaction rate with power, even though d^+ ions start to become unconfined at 2.5 times lower energy than $^3He^{++}$ ions.

C. COMPARISON WITH REACTION RATE MODEL

The predictions of the reaction rate model described earlier have been compared with the measured rates. The predicted d-^{3}He rate was sensitive to the power deposition profile width of the ICRF fast wave, the minority ion density, and the electron temperature. The power deposition width was not known experimentally, while the minority density was measured only during ohmic heating and could be affected by a different wall source or recycling rate during ICRF heating. Within the uncertainties, the observed rates are consistent with the predictions of the model.

In applying the model, several experimental quantities were used as inputs. The ICRF power was calculated from the forward power produced at the source times the ratio of plasma loading resistance and total resistance which includes losses in the transmission line and vacuum vessel; it was typically 80% to 90% of the forward power. The line-averaged electron density was measured by a microwave interferometer. The ion temperature was measured from the neutron emission and by a mass-sensitive, charge-exchange diagnostic. The electron temperature was measured by Thomson scattering. The majority deuterium density was calculated using $Z_{eff} = 3$ due mainly to carbon impurities. The density and

temperature profiles were typically $n_e(r) \approx 1.5\ \bar{n}_e\ (1 - (r/a)^2)$ and $T(r) = T(0)\ (1 - (r/a)^2)^2$.

The d-^{3}He rate predicted by the model rose strongly with ICRF power. For constant power deposition width and ^{3}He density, the model predicted a faster rise with power ($\propto P_{RF}^{5.5}$) than observed experimentally ($\propto P_{RF}^{3.4}$ at constant density). The difference may be due to the limitation of the model in overestimating the power deposited in the ^{3}He tail for finite $k_\perp \rho_{^3He}$ (about0.5 for PLT). The experimental measurements were reproduced either by using a power deposition width which increased with power or a ^{3}He density which increased with power. For example, the gaussian width σ of the power deposition profile must be increased from 9.5 cm at 0.4 MW to 12.5 cm at 1.0 MW for $\bar{n}_{^3He} = 1.2 \times 10^{12}$ cm^{-3}, or $\bar{n}_{^3He}$ must be increased from 1.2×10^{12} cm^{-3} at 0.4 MW to 2.1×10^{12} cm^{-3} at 1.0 MW for $\sigma = 9.5$ cm to match the experimental scaling.

The model predicted a decrease of d-^{3}He rate with electron density as $n_e^{-4.3}$. The experimental scaling was reproduced by assuming a modest increase with density of T_e (.87 → 1.0 keV, within the experimental uncertainty), or a decrease in $\bar{n}_{^3He}$ (.12 → .10 $\times 10^{13}$ cm^{-3}) or σ (10.7 → 9.8 cm).

The predicted variation of the d-^{3}He rate with T_e was in agreement with the measurement. For $\bar{n}_{^3He} = 1.0 \times 10^{12}$ cm^{-3} and $\sigma = 9.7$ cm , an increase in T_e from 1.5 to 1.8 keV increased the d-^{3}He rate from 1.4×10^{13} s^{-1} to 3.7×10^{13} s^{-1} at $\bar{n}_e = 4.0 \times 10^{13}$ cm^{-3}, similar to Figure 7.

The model predicted that ^{3}He orbit losses become important above 1700 keV (850 keV) for 500 kA (340 kA) plasma current. The d-^{3}He reactivity reaches 90 % of its asymptotic level by 550 keV for the highest emission level observed. Hence no saturation in d-^{3}He rates with power due to orbit losses was expected, consistent with the power scans at full and 70% plasma current. The difference in d-^{3}He rates for the two cases could be modeled by an electron temperature

decrease (1.7 → 1.5 keV) or an increase in $\bar{n}_{^3He}$ (.12 → .14 × 10^{13} cm^{-3}) or σ (11.8 → 12.6 cm).

We also modeled the m=2 and sawtooth discharge comparison. Based on the measured $\bar{n}_e$ and T_e, the model predicted 20% lower d-^{3}He rates during the m=2 case, whereas the m=2 case was actually 60% lower. The difference may have been due to a broader power deposition profile, higher ^{3}He density, or poorer energetic ^{3}He confinement or acceleration during the m=2 case.

We examined the case of d^+ minority heating in a ^{3}He plasma using the reaction rate model. The power scan data [Figure 15(b)] could be reproduced in a manner similar to the ^{3}He minority power scan case. For σ = 11.1 cm, we needed $\bar{n}_d$ = 1.5 × 10^{12} cm^{-3} at 220 kW, increasing to 3.2 × 10^{12} cm^{-3} at 665 kW. For constant $\bar{n}_d$ = 1.5 × 10^{12} cm^{-3}, we needed σ = 11.1 cm at 220 kW increasing to σ = 16.0 cm at 665 kW.

VI. d-^{3}He TIME EVOLUTION

The time evolution of the d-^{3}He reaction rate during ^{3}He minority heating was measured using the proton probe. The general features of the time evolution included the rise and fall times of the d-^{3}He rate at the beginning and end of the RF heating. Oscillations in the reaction rate included sawtooth and m=2 activity. Large sawtooth oscillations (20% drop) accompanied the largest reaction rate conditions. Ten percent amplitude, 0.5 - 1.5 kHz oscillations in the reaction rate were correlated with n=1, m=2 MHD activity and were acccompanied by a 50% drop in the reaction rate.

A. GENERAL FEATURES

The general features of the d-^{3}He time evolution are illustrated in Figure 9 for one of the highest reaction rate cases. The ^{3}He gas puff occurred from 350 to 393 ms and caused a rise in the electron density beginning at 380 ms. The forward power from the ICRF amplifier was turned on at 420 ms and reached 850 kW at 450 ms. The ICRF power absorbed by the plasma reached 780 kW or about 90% of the forward power.

The d-^{3}He reaction rate began to rise when the ICRF power reached its maximum level. After 10-20 ms, the d-^{3}He rate rose linearly ($\propto t/\tau_R$) or as $[1 - \exp(-t/\tau_R)]$, characterized by a rise time τ_R. The d-^{3}He rate rose more slowly with the onset of sawtooth oscillations until reaching a steady average level. The d-^{3}He rate dropped as $\exp(-t/\tau_D)$ with a decay time τ_D when the ICRF power was turned off.

The d-^{3}He rise time varied from 20 to 65 ms which was comparable to (somewhat greater than) the ion (electron) energy confinement time. τ_R showed no correlation with ICRF power, but tended to decrease with electron density approximately as n_e^{-1} [Figure 10(a)]. Discharges with m=2 activity in the plasma tended to have shorter τ_R than discharges with sawtooth activity [Figure 10(b)].

The decay time τ_D of the d-^{3}He rate varied between 2 and 8.5 ms. τ_D was correlated with the slowing down rate of the energetic ^{3}He ions. These ^{3}He ions slowed down due to electron drag since their energy was much greater than the critical energy (28 T_e) where electron and deuteron drags are equal. We found that τ_D was proportional to the central ^{3}He energy loss time due to electron drag, $\nu_E(0)^{-1}$, where $\nu_E(0) \propto n_e T_e^{-3/2}$ was the central ^{3}He energy loss rate

(Figure 11). The error bar reflected a 100 eV uncertainty in T_e. We found that $\tau_D = K_1 \nu_E(0)^{-1}$ where K_1 was between 0.13 and 0.30.

The central ^{3}He energy loss time is an overestimate of the average energy loss time of the ^{3}He ions. The calculated volume- weighted d-^{3}He emission was peaked at about 8 cm and the banana width of the ^{3}He ions (10 cm for 200 keV ^{3}He) causes them to sample plasma away from the center. The energy loss time at 15 cm was 0.74 $\nu_E(0)^{-1}$ for typical electron temperature and density profiles $\{T_e \propto [1 - (r/a)^2]^2, \; n_e \propto [1 - (r/a)^2]\}$. Taking 15 cm for the average energy loss radius, we would find $\tau_D = K_2 \nu_E(15)^{-1}$ where K_2 was between 0.18 and 0.40. The ^{3}He energy loss time was also reduced by the decay of the electron temperature after the ICRF heating.

The decay time τ_D is expected to be shorter than ν_E^{-1} due to the steepness of the d-^{3}He cross section with energy in the energy range of interest. The reaction rate should drop by 1/e when the ^{3}He ions have slowed down enough for their cross sections to decrease by 1/e. In Figure 12 we show the variation of the fractional d-^{3}He decay time $\tau_D \nu_E$ with ^{3}He energy predicted from the energy dependence of the cross section. This figure shows that the observed decay times imply that the d-^{3}He reactions were caused by ^{3}He ions with energies in the range of 100-400 keV.

B. d-^{3}He SAWTOOTH OSCILLATIONS

The largest d-^{3}He reaction rates which we observed were accompanied by large (up to 20% drop) sawtooth oscillations in the proton probe signal. These proton sawteeth occurred together with the soft x-ray sawteeth. The decay time of the sawtooth drop varied from 50 μs at the highest reaction rates and low density to several ms at lower reaction rates and higher ($\simeq 4 \times 10^{13}$ cm^{-3}) density.

However, the proton sawteeth were never observed using the proton spectrometer which had a broader spatial sensitivity (Figure 3) and presumably integrated the emission over the radial extent of the sawtooth.

The rapid sawtooth drop at low densities could not be understood in terms of the ^{3}He collisional energy loss rate ν at the time of the sawtooth. The d-^{3}He reaction rate should evolve to a new equilibrium level with a decay rate of about 5ν due to the steep energy dependence of the cross section. Even if the electron temperature dropped 50% in a sawtooth with no change in density, the collisional decay time would be about 0.7 ms or longer which cannot explain the fast low density sawtooth drop.

The proton sawteeth are illustrated (Figure 13) for a moderate density ($\bar{n}_e = 2.6 \times 10^{13}$ cm^{-3}) and reaction rate (4.3×10^{12} s^{-1}) case at 820 kW ICRF power, together with the neutron and central soft x-ray traces (both inverted). The soft x-ray sawteeth had a drop of about 45% and a period of 12 ms. The proton emission dropped as much as 20% with decay times between about 0.5 and 2 ms. The volume-integrated neutron signal also showed sawtooth oscillations which were smaller in amplitude ($\simeq$10%) and had a longer decay (3-4 ms). The proton emission dropped immediately when the ICRF power was turned off, but the neutron emission did not begin to drop until the next sawtooth occurred. This indicated that the energetic ^{3}He ions producing the proton emission were far above the critical energy and contributed a negligible amount of heating to the deuterons as reflected in the neutron emission. The effect of the last sawtooth in Figure 13 was seen on the proton signal as an increase in the decay rate.

A low density, high reaction rate case was shown in Figure 9. The sawtooth decay was smaller in amplitude (10%) and faster (0.1-0.3 ms), compared to the decay of the emission at the end of the ICRF heating (τ_D = 5.3 ms).

In the fastest sawtooth decay that we have observed [Figure 14(a)], the proton emission dropped by 10% in 50 μs. The soft x-ray signal [Figure 14(b)] showed a similar decay time. The conditions for this case were $\bar{n}_e = 1.9 \times 10^{13}$ cm^{-3}, $\bar{n}_{^3He} = 1 \times 10^{12}$ cm^{-3}, and 740 kW of ICRF power.

Measurements of the d-^{3}He reaction rate using the proton spectrometer in the current mode showed no proton sawteeth. The difference in d-^{3}He time evolutions measured by the two detectors was probably due to their differing spatial sensitivities. The calculated detector efficiencies (Figure 2) showed that the proton probe efficiency was peaked inside 5 cm minor radius while the proton spectrometer efficiency was peaked at 11 cm and extended out to 22 cm. These calculations showed that the proton probe was especially sensitive to the central emission while the proton spectrometer tended to average over the emission region out to 22 cm.

A possible explanation of the rapid sawtooth decay times was that the energetic ^{3}He ions were spatially rearranged in the region near the q=1 surface (r = 10 cm). The decrease of the proton probe signal could have resulted from movement of some ^{3}He ions to regions of smaller detection efficiency. The proton spectrometer would continue to detect the reactions caused by those ions in the plasma outside the q=1 surface due to its broader spatial sensitivity.

C. d-^{3}He m=2 OSCILLATIONS

Oscillations in the d-^{3}He reaction rate also occurred during discharges with m=2 poloidal magnetic perturbations. These discharges typically had poorer thermal plasma confinement and occurred less often than sawtooth discharges.

An example of the d-^{3}He reaction rate during an m=2 discharge is shown (Figure 15). The d-^{3}He reaction rate oscillations reached a maximum amplitude of about 10%. Oscillations in the d-^{3}He rate, soft x-ray chord, and m=2 magnetic signal all decreased in frequency together. The time scales of these signals agreed to within 0.1 ms.

The mode numbers of the magnetic islands were identified using three soft x-ray detector arrays. The magnetic island was identified as m=-2, n=1 where the poloidal mode rotation was in the electron diamagnetic direction.

The phase information for the diagnostics as well as the ICRF coils (Table 1) was used to determine the orientation of the magnetic island at the ICRF coils. The o-points (regions of highest x-ray emission) of the island were located on the horizontal midplane between the ICRF coils after a phase lag of 30° with respect to the x-ray chord (r=25 cm) shown in Figure 15 and with a phase lead of 140° with respect to the maximum of the m=2 magnetic signal. The magnetic signal incorporated an active integrator with an RC time constant of 4 ms so its phase information was accurate only for 1 kHz or greater oscillation frequencies. Comparison of the d-^{3}He rate and x-ray chord signal during the slow island rotation in Figure 15 showed that the d-^{3}He rate was largest when the island had the horizontal orientation near the ICRF coils. For faster island rotation, the d-^{3}He rate peaked 0.3 to 0.4 ms (or about 180°) after the island was horizontal near the ICRF coils. In addition, the amplitude of the d-^{3}He oscillation was smaller during the faster rotation. The m=2 magnetic signal maintained the expected ≈170° phase lag with respect to the x-ray signal for oscillation frequency above 1 kHz, confirming the island orientation already described.

Based on the d-^{3}He rise time (20 ms) at the beginning of ICRF heating, the time for the d-^{3}He rate to rise by 20% was 4 ms, while the decay time after the ICRF pulse implied a 20% drop in about 0.8 ms. The oscillation period during the fast island rotation was about 1 ms or about one-fourth of the acceleration time. Therefore the ion distribution could not reach a new equilibrium if the d-^{3}He oscillations were caused by m=2 power modulations at the oscillation frequency. Such changes in the ICRF power by the m=2 mode are possible due to changes in the plasma (and ICRF coupling) in the vicinity of the ICRF coils.

These proton oscillations might also be due to changes in the ^{3}He orbits in the presence of the m=2 island, thereby modulating the detector efficiency. The o-point of the magnetic island was near the proton detector about 150° ahead of the maximum soft x-ray signal. The proximity occurred about 90° after the peak in the proton signal during slow island rotation.

VII. DISCUSSION

The d-^{3}He reaction measurements during ^{3}He minority ICRF heating provide direct evidence for the formation of a supra-thermal ^{3}He distribution. A lower limit on the ^{3}He energies can be estimated assuming that the ^{3}He ions are monoenergetic. For the measured ^{3}He and deuterium densities, the maximum reaction rate of about 1.7×10^{14} s^{-1} implies an energy of 100 keV for the ^{3}He ions.

The reaction rate can provide another estimate, assuming that the ^{3}He energy distribution was described by the quasilinear velocity space diffusion theory. Our reaction rate model based on this theory predicted that most of the d-^{3}He reactions were due to ^{3}He ions in the range of 300-400 keV. This estimate

depends on the magnitude of the reaction rate and is not affected by uncertainties in the power deposition and ^{3}He density.

The d-^{3}He proton energy spectrum provides another estimate of the ^{3}He energies. In an experiment at 350 kW ICRF power, the proton spectrum had a FWHM of 2.3 MeV, which corresponds to a reacting ^{3}He energy of at least 190 keV.

A fourth estimate of the reacting ^{3}He energies was obtained from the measured d-^{3}He decay times. The decay times were consistent with the slowing down of 100-400 keV ^{3}He ions.

The ^{3}He energies in the range of several hundred keV provide an estimate of the ^{3}He particle confinement time during ICRF heating. ^{3}He ions gained an average energy increment ΔE for each pass through the resonance layer, given by

$$\Delta E = (1/2)(2\pi r/v_\theta)(\langle P\rangle/n_{^3He})$$

where v_θ is the θ-component of the parallel velocity and $\langle P\rangle$ is the ICRF power density. The ^{3}He ions cross the resonance layer twice per poloidal transit, so the minimum time required to gain an energy E was $E\, n_{^3He}/\langle P\rangle$. For a typical ^{3}He density (1×10^{12} cm^{-3}) and power density (1 W cm^{-3}), the minimum confinement time was 16 ms to reach 100 keV and 64 ms to reach 400 keV. These estimates are similar to the d-^{3}He rise times observed.

VIII. CONCLUSIONS

The energy of the reacting minority ions during fast wave heating was determined from measurements of the d-^{3}He fusion reaction rates and the energy spectrum of the escaping protons. The d-^{3}He reactions produced during 0.4 to 1.0 MW ^{3}He minority heating are due to ^{3}He ions in the range of 100-400 keV. These energies further implied energetic ^{3}He confinement in the range of 15 to 60 ms or better. The d-^{3}He fusion power (0.2-1.5 kW) and fusion multiplication

(2×10^{-4} + 1.5×10^{-3}) are the highest in any controlled fusion experiment to date. The scalings of the d-^{3}He reaction rate with density, temperature, and ICRF power are consistent with a one-dimensional reaction rate model based on the minority distribution predicted from quasilinear RF-diffusion theory.

Sawtooth and m=2 oscillations are observed in the d-^{3}He proton emission. The rapid sawtooth drop, much faster than the energetic ^{3}He energy loss time, was suggestive of expulsion or redistribution of these ions from the plasma center. The m=2 oscillations were observed in the presence of a rotating magnetic island structure.

ACKNOWLEDGMENTS

The authors thank W. Stodiek, J. Hosea, H. Eubank, and the PLT experimental and technical groups for their support. They are grateful to G. Estepp for technical assistance. Valuable discussions with P. Colestock, D. Hwang, J. R. Wilson, H. R. Thompson, and Cris W. Barnes are also acknowledged. The soft X ray and magnetic loop measurements were provided by J. R. Wilson. We thank W. Heidbrink for help in determining the proton detector efficiencies.

This work was supported by U S Department of Energy Contract No. DE-AC02-76-CHO-3073.

REFERENCES

[1]J. Adam, M. Chance, H. Eubank, W. Getty, E. Hinnov, W. Hooke, J. Hosea, F. Jobes, F. Perkins, R. Sinclair, J. Sperling, H. Takahashi, in Plasma Physics and Controlled Nuclear Fusion Research (International Atomic Energy Agency, Vienna, 1974) p. 65.

[2]H. Takahashi, C. C. Daughney, R. A. Ellis, Jr., R. J. Goldston, H. Hsuan, T. Nagashima, F. J. Paoloni, A. J. Sivo, S. Suckewer, Phys. Rev. Lett. 39, 31 (1977).

[3]V. L. Vdovin, N. N. Shapotkovskii, A. V. Shesnikow, Proceedings 8th International Conference on Controlled Fusion and Plasma Physics, I, 19 (1978).

[4]J. C. Hosea, S. Bernabei, P. L. Colestock, S. L. Davis, P. C. Efthimion, R. J. Goldston, D. Q. Hwang, S. S. Medley, D. Mueller, J. D. Strachan, H. R. Thompson, Phys. Rev. Lett. 43,1802 (1979).

[5]J. Hosea, D. Boyd, N. Bretz, R. Chrien, S. Cohen, P. Colestock, S. Davis, D. Dimock, P. Efthimion, H. Eubank, R. Goldston, L. Grisham, E. Hinnov, D. Hwang, F. Jobes, D. Johnson, R. Kaita, J. Lawson, E. Mazzucato, D. McNeill, S. Medley, E. Meservey, D. Mueller, G. Schilling, J. Schivell, G. Schmidt, A. Sivo, F. Stauffer, W. Stodiek, J. Strachan, S. Suckewer, G. Tait, H. Thompson, G. Zankl, in Plasma Physics and Controlled Nuclear Fusion Research (International Atomic Energy Agency, Vienna, 1981) p. 95.

[6]V. P. Bhatnagar, G. Bosia, E. Desoppere, P. D'Hondt, R. Koch, A. M. Messiaen, J.-M. Noterdaeme, D. Pearson, G. Poulaert, R. M. Prates-Drozak, G. Telesca, P. E. Vandenplas, G. Van Oost, G. Van Wassenhove, R. R. Weynants, in Plasma Physics and Controlled Nuclear Fusion Research (International Atomic Energy Agency, Vienna, 1981) p. 85.

[7]Equipe TFR, in Plasma Physics and Controlled Nuclear Fusion Research (International Atomic Energy Agency, Vienna, 1981) p. 75

[8]H. Kimura, K. Odajima, S. Iizuka, S. Sengoku, T. Sugie, K. Takahashi, H. Takeuchi, T. Yamauchi, K. Kumagai, H. Matsuda, K. Ohasa, S. Yamamoto, K. Anno, T. Shibata, H. Sunaoshi, H. Hiratsuka, K. Yokoyama, A. Funahashi, T. Nagashima, H. Maeda, Y. Shimomura, in Plasma Physics and Controlled Nuclear Fusion Research (International Atomic Energy Agency, Vienna, 1981) p. 105.

[9]R. J. Taylor, P. Lee, N. C. Luhmann, Jr., A. Mase, G. J. Morales, W. A. Peebles, A. Semet, F. Schwirzke, S. Talmadge, S. J. Zweben, M. A. Hedemann, B. S. Levine, R. W. Gould, in Plasma Physics and Controlled Nuclear Fusion Research (International Atomic Energy Agency, Vienna, 1981) p. 61.

[10]Equipe TFR, in Plasma Physics and Controlled Nuclear Fusion Research (International Atomic Energy Agency, Vienna, 1981) p. 425.

[11]R. E. Chrien, P. L. Colestock, H. P. Eubank, J. C. Hosea, D. Q. Hwang, J. D. Strachan, H. R. Thompson, Jr., Phys. Rev. Lett. 46, 535 (1981).

[12]S. Yoshikawa, M. A. Rothman, R. M. Sinclair, Phys. Rev. Lett. 14, 214 (1965).

[13]P. L. Colestock, S. L. Davis, J. C. Hosea, D. Q. Hwang, H. R. Thompson, Heating in Toroidal Plasmas (2nd Joint Grenoble-Varenna International Symposium, Belgium, 1980), 1, 471.

[14]T. H. Stix, Nucl. Fusion 15, 737 (1975).

[15]C. F. Kennel, F. Engelmann, Phys. Fluids 9, 2377 (1966).

[16]B. H. Duane, Battelle Pacific Northwest Laboratories, BNWL-1685 (1972).

[17]R. J. Goldston, Ph.D. Thesis, Princeton University (1977), Chapter 2, p. 16.

[18]R. E. Chrien, H. P. Eubank, D. M. Meade, J. D. Strachan, Nucl. Fusion 21, 1661 (1981).

[19]J. D. Strachan, P. L. Colestock, S. L. Davis, D. Eames, P. C. Efthimion, H. P. Eubank, R. J. Goldston, L. R. Grisham, R. J. Hawryluk, J. C. Hosea, J. Hovey, D. L. Jassby, D. W. Johnson, A. A. Mirin, G. Schilling, R. Stooksberry, L. D. Stewart, H. H. Towner, Nucl. Fusion 21, 67 (1981).

[20]H. H. Anderson, J. F. Ziegler, Hydrogen Stopping Powers and Ranges in All Elements, Pergamon Press (1977).

[21]H. H. Towner, D. L. Jassby, Trans. Am. Nucl. Soc. 22, 74 (1975).

TABLE 1

Device	ϕ	θ	$\psi=\phi-2\theta$	$\psi_{observed}$
m = 2 magnetic signal	40^o	0^o	40^o	40^o(fast)
x-ray (top) central chord	70^o	90^o	-110^o	-110^o
x-ray (top) central chord	-30^o	90^o	-210^o	-210^o
x-ray (side) r=25 cm chord	-30^o	60^o	-150^o	-150^o
Proton probe	0^o	0^o	0^o	180^o(slow)
				0^o(fast)
ICRF Coil	170^o	0^o	170^o	--
ICRF Coil	190^o	0^o	190^o	--

Table 1: Toroidal (measured clockwise from proton probe) and poloidal (measured from outer horizontal midplane) angle locations of the diagnostics and ICRF coils shown in Figure 25, together with their phase relationships with respect to a n = 1 m = -2 helical magnetic island structure. The observed phases are with respect to the midplane location between the ICRF coils for both fast and slow island rotation.

FIGURE CAPTIONS

Figure 1. Calculated ^{3}He minority distribution function near the plasma center during ICRF heating for one of the highest reaction rate cases and variation of d-^{3}He reactivity with maximum ^{3}He energy for this distribution.

Figure 2. (a) Proton probe used for time-resolved d-^{3}He reaction measurements which was inserted into the vacuum vessel in the horizontal midplane. (b) Details of the proton spectrometer used for energy-resolved d-^{3}He measurements located at the bottom of the vacuum vessel.

Figure 3. Differential detector efficiency $d\epsilon/d\ell$ as a function of minor radius for the (a) proton probe and (b) proton spectrometer.

Figure 4. d-^{3}He proton spectrum during deuterium neutral beam injection into a deuterium plasma containing a small concentration of ^{3}He, together with the predicted spectrum.[21]

Figure 5. d-^{3}He proton spectra during ICRF heating for a plasma current of (a) 500 kA and (b) 250 kA.

Figure 6. (a) Variation of proton emission with $\bar{n}_e$ showing decrease $\propto \bar{n}_e^{-3}$. (b) Variation of proton emission with ICRF power for two values of the plasma current.

Figure 7. Variation of the d-^{3}He rate with density for two electron temperatures.

Figure 8. (a) Variation of d-^{3}He and d-d rates with central magnetic field, and therefore with major radius (R_c) of the cyclotron layer. (b) Variation of d-^{3}He and d-d rates with ICRF power.

Figure 9. Time evolutions of the d-^{3}He reaction rate, input ICRF power absorbed by the plasma, and electron density.

Figure 10. (a) Variation of d-^{3}He rise time τ_R with electron density showing $\tau_R \propto \bar{n}_e^{-1}$. (b) Variation of τ_R with density for m=2 and sawtooth discharges.

Figure 11. Variation of d-^{3}He decay time with central energy loss time ν_E^{-1} for ^{3}He ions due to electron drag.

Figure 12. Fraction of the ^{3}He energy loss time required for the d-^{3}He reaction rate to drop by 1/e as a function of ^{3}He ion energy.

Figure 13. Time evolution of the d-^{3}He proton signal and the central soft X ray and neutron signals (inverted).

Figure 14. Time evolutions of (a) d-^{3}He rate and (b) central soft x-ray detector signal during a fast sawtooth decay.

Figure 15. Time evolutions of d-^{3}He rate, soft x-ray (r = 25 cm) chord, and m = 2 magnetic loop signal during an m = 2 discharge.

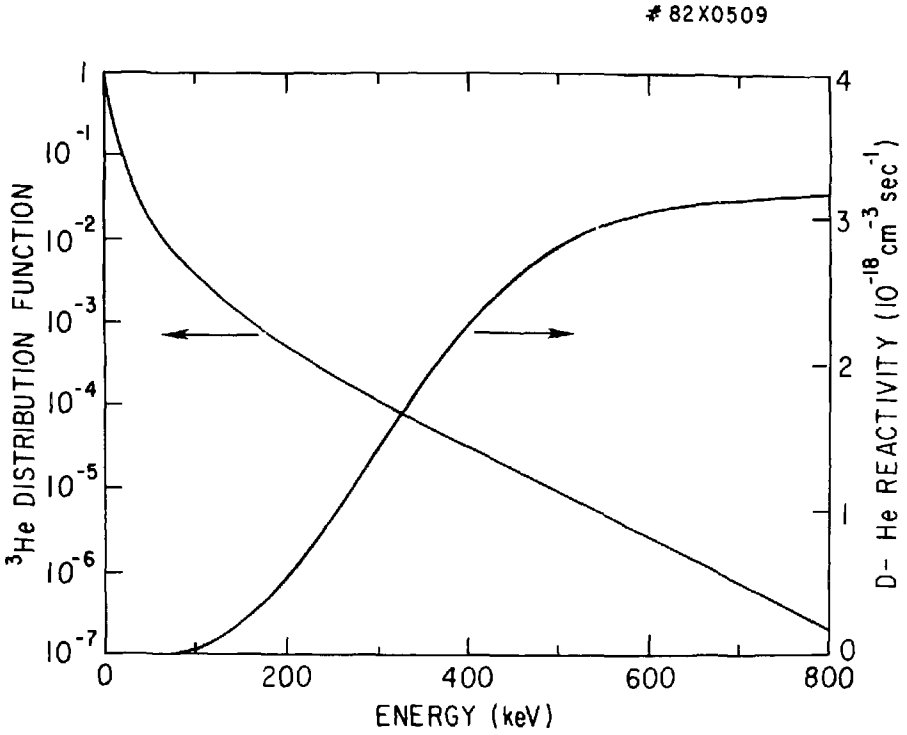
#82X0509
^{3}He DISTRIBUTION FUNCTION
D- He REACTIVITY (10^{-18} cm^{-3} sec^{-1})
ENERGY (keV)
1
10^{-1}
10^{-2}
10^{-3}
10^{-4}
10^{-5}
10^{-6}
10^{-7}
0
200
400
600
800
4
3
2
1
0

Fig. 1

#82X0511

(a) PROTON PROBE

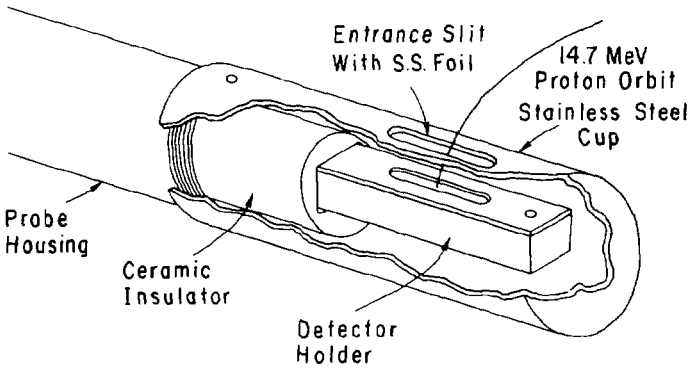

(b) PROTON SPECTROMETER

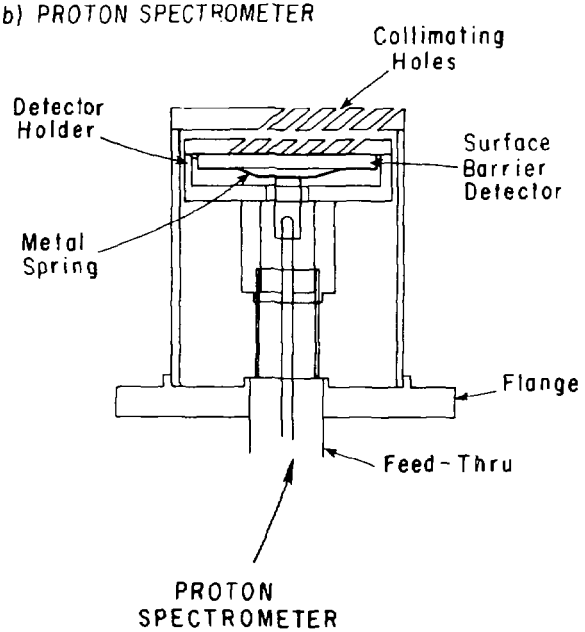

Fig. 2

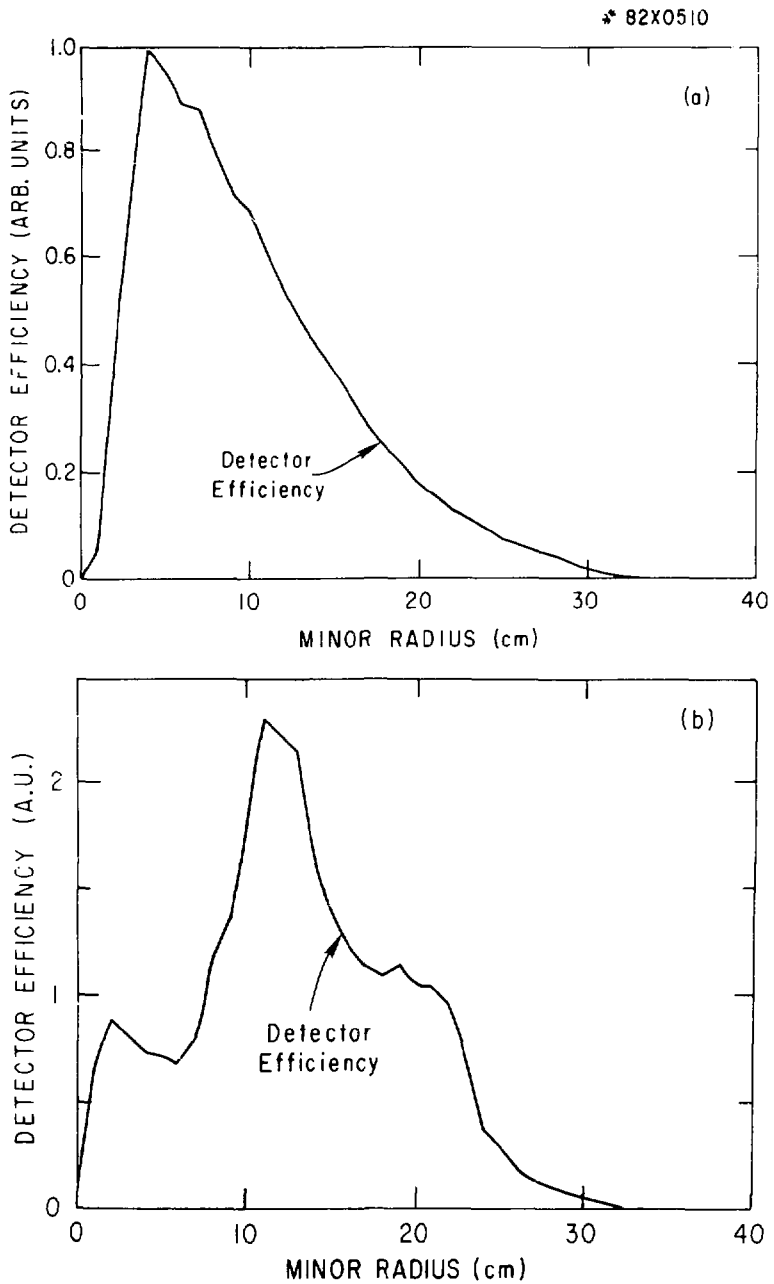
82X0510
(a)
DETECTOR EFFICIENCY (ARB. UNITS)
1.0
0.8
0.6
0.4
0.2
0
Detector
Efficiency
0
10
20
30
40
MINOR RADIUS (cm)
(b)
DETECTOR EFFICIENCY (A.U.)
2
1
0
Detector
Efficiency
0
10
20
30
40
MINOR RADIUS (cm)

Fig. 3

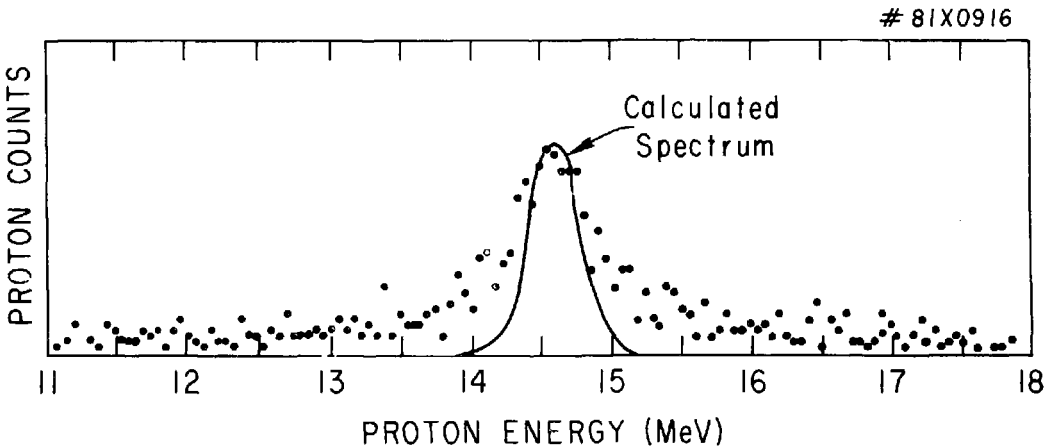
#81X0916
PROTON COUNTS
Calculated
Spectrum
11
12
13
14
15
16
17
18
PROTON ENERGY (MeV)

Fig. 4

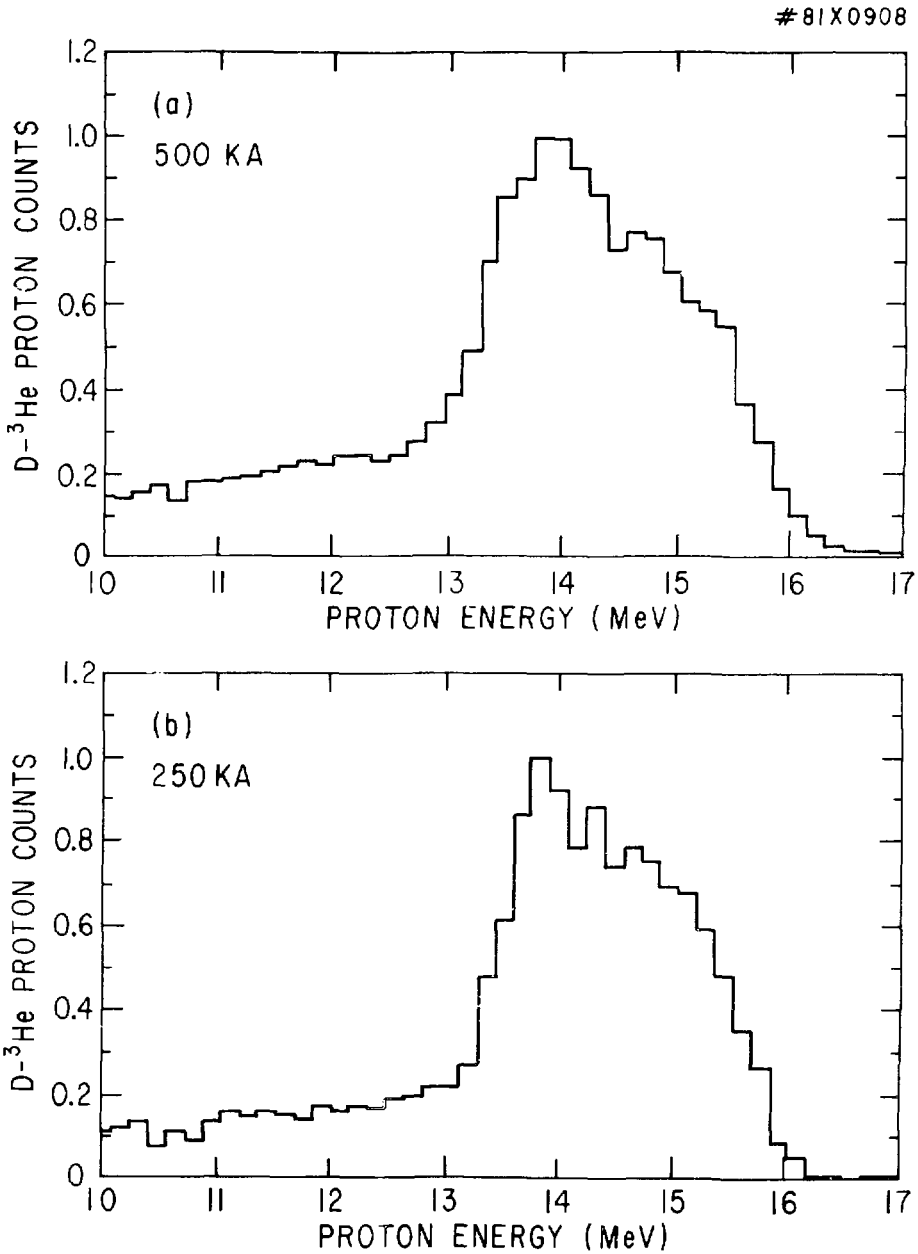
#81X0908
(a)
500 KA
D-3He PROTON COUNTS
PROTON ENERGY (MeV)
(b)
250 KA
D-3He PROTON COUNTS
PROTON ENERGY (MeV)

Fig. 5

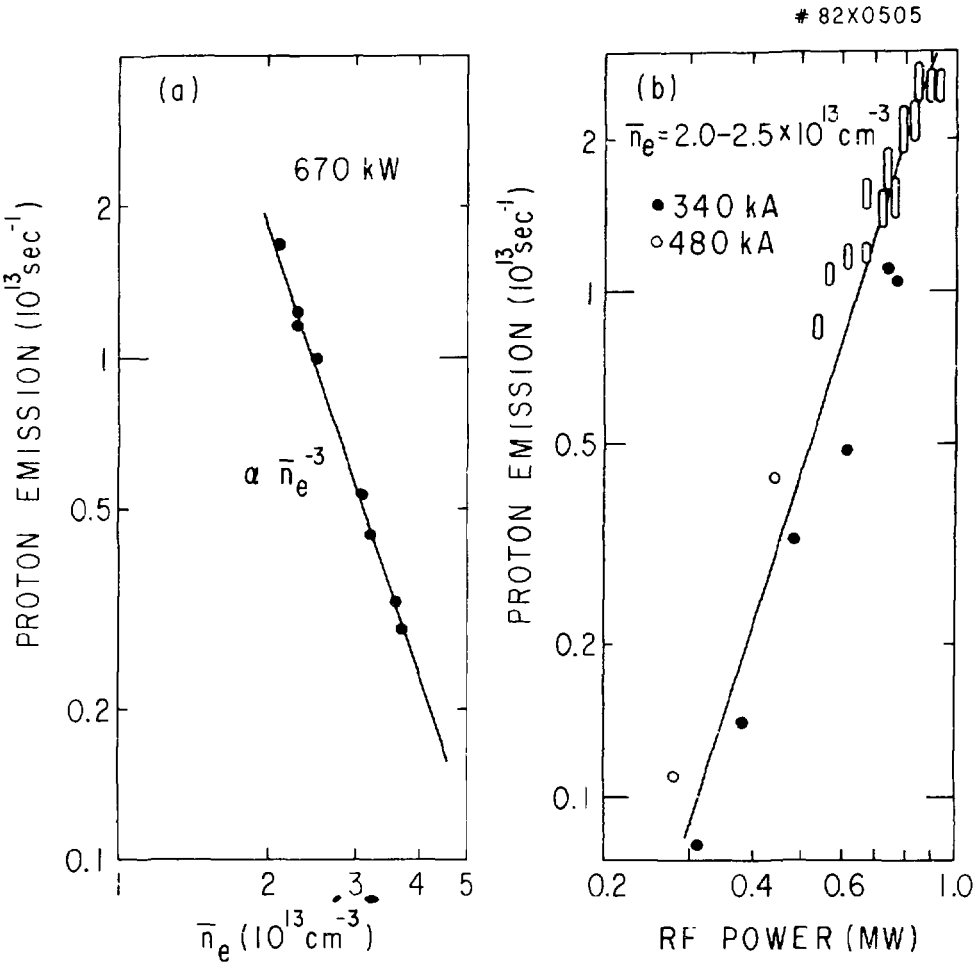
82X0505
(a)
670 kW
$\alpha\ \bar{n}_e^{-3}$
PROTON EMISSION (10^{13}sec^{-1})
$\bar{n}_e$ (10^{13}cm^{-3})
(b)
$\bar{n}_e$=2.0-2.5x10^{13}cm^{-3}
• 340 kA
○ 480 kA
PROTON EMISSION (10^{13}sec^{-1})
RF POWER (MW)

Fig. 6

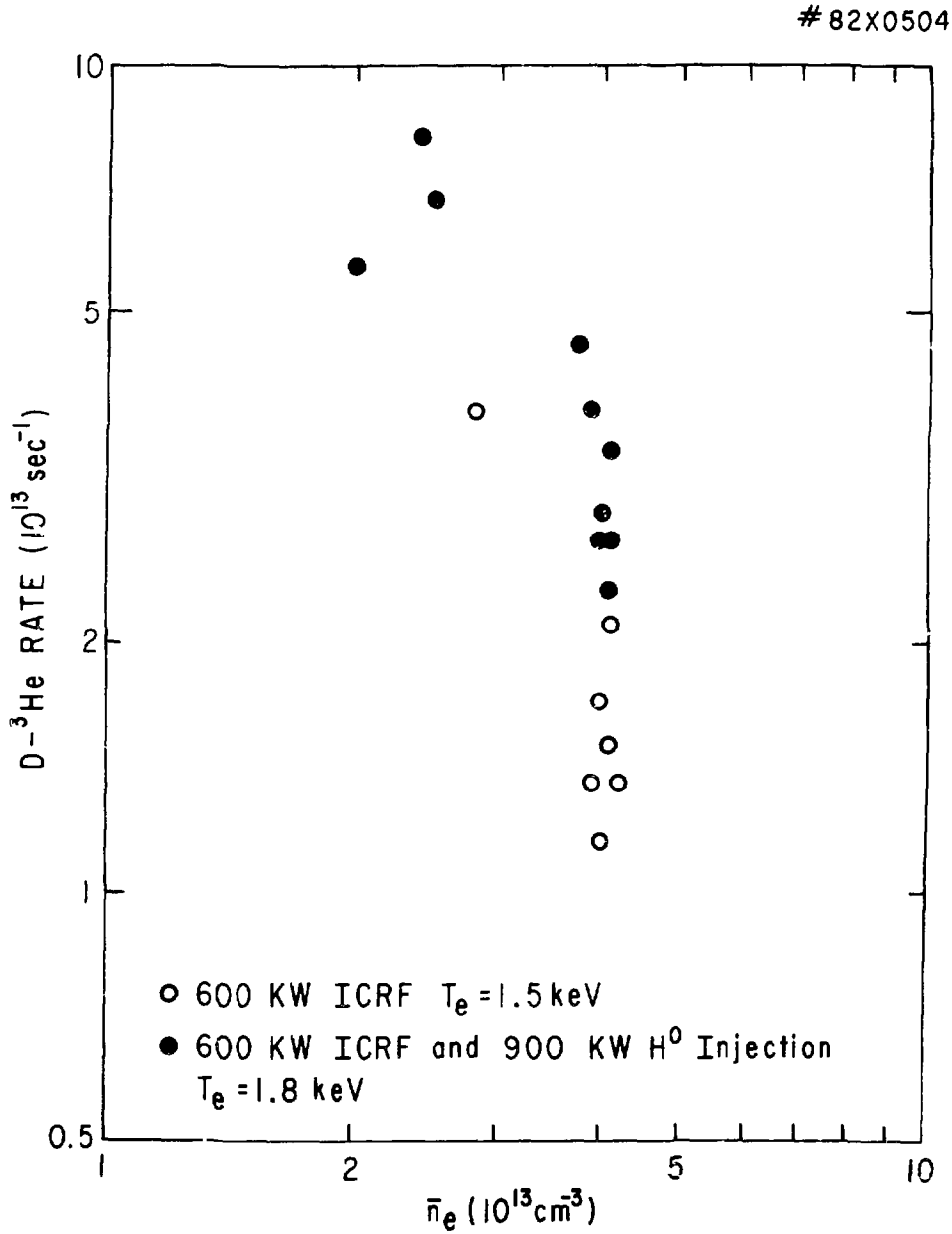
#82X0504
10
5
2
1
0.5
D-³He RATE (10¹³ sec⁻¹)
1
2
5
10
n̄e (10¹³cm⁻³)
○ 600 KW ICRF Te = 1.5 keV
● 600 KW ICRF and 900 KW H⁰ Injection
Te = 1.8 keV

Fig. 7

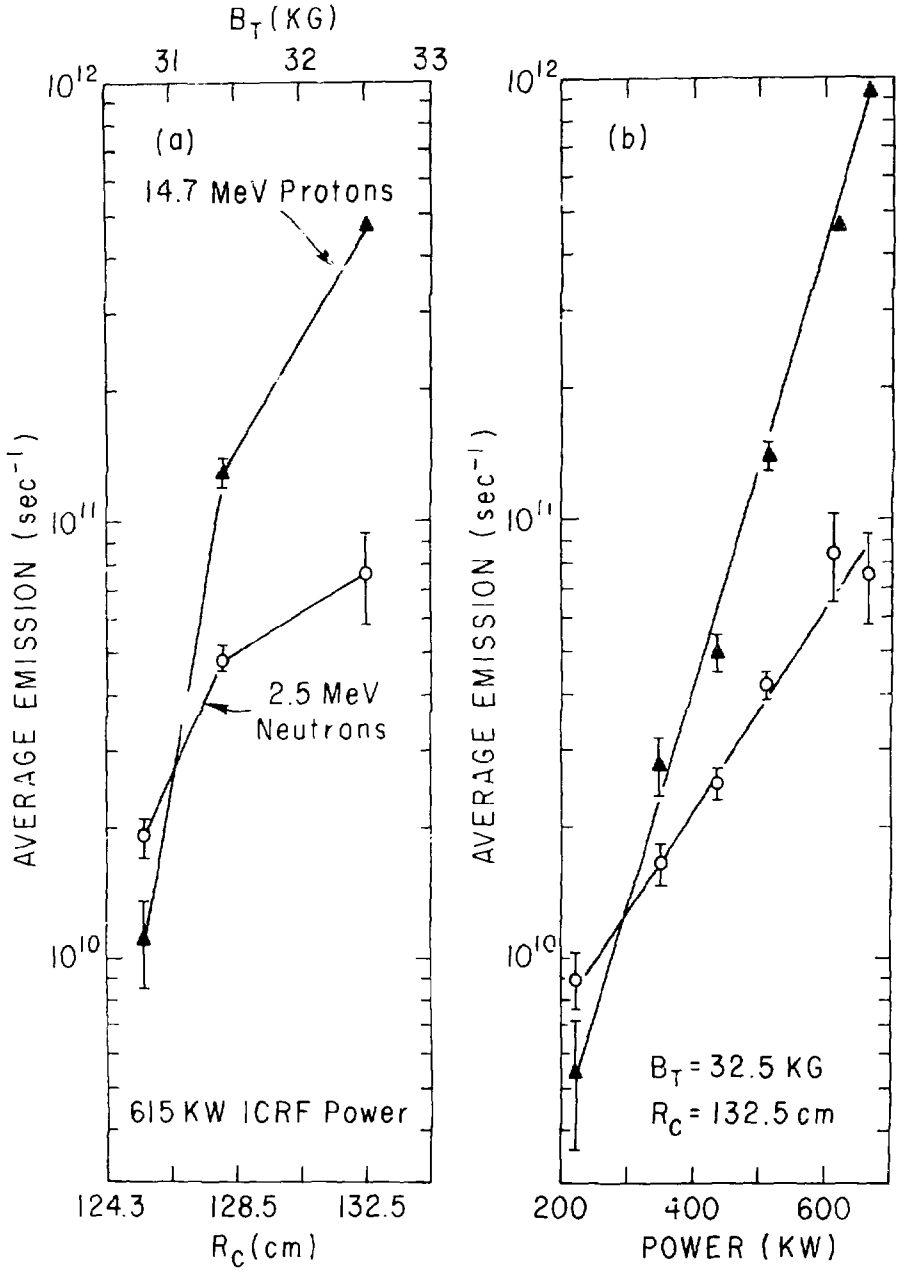
B_T (KG)
31
32
33
10^{12}
(a)
14.7 MeV Protons
10^{11}
10^{10}
AVERAGE EMISSION (sec^{-1})
2.5 MeV
Neutrons
615 KW ICRF Power
124.3
128.5
132.5
R_C (cm)
(b)
B_T = 32.5 KG
R_C = 132.5 cm
200
400
600
POWER (KW)

Fig. 8

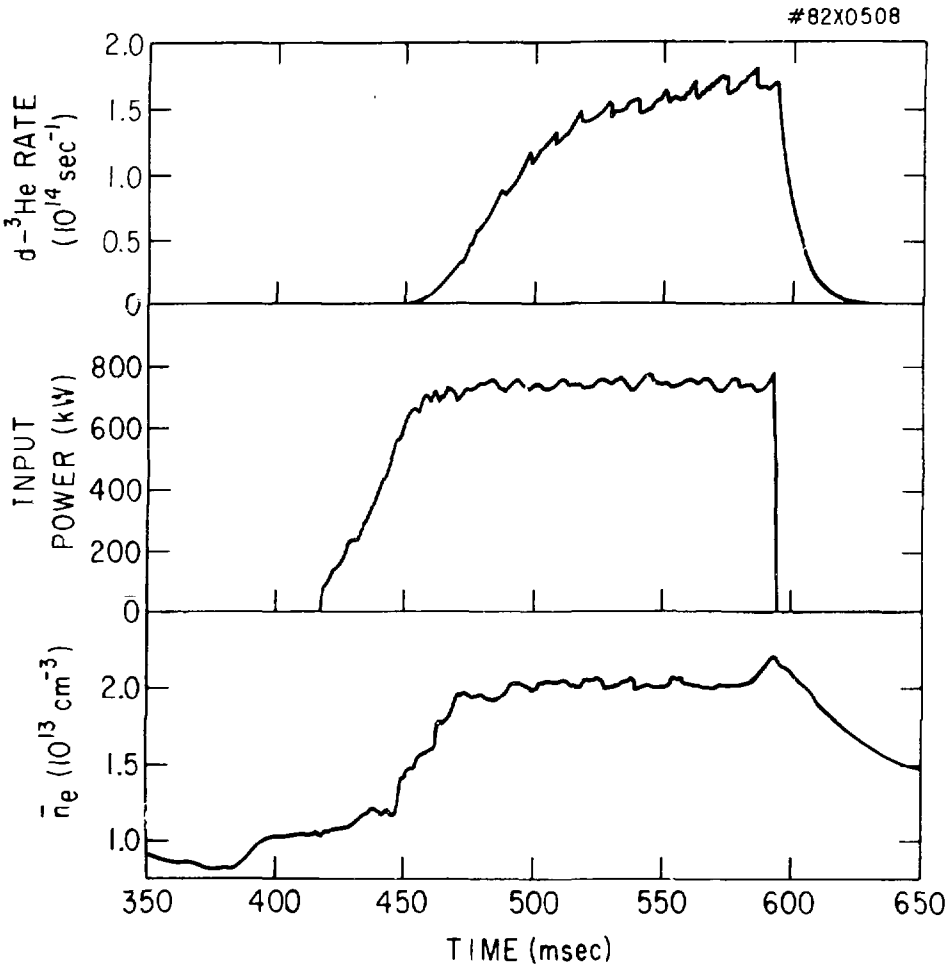
#82X0508
d-3He RATE (10^14 sec^-1)
2.0
1.5
1.0
0.5
0
INPUT POWER (kW)
800
600
400
200
0
n̄e (10^13 cm^-3)
2.0
1.5
1.0
350
400
450
500
550
600
650
TIME (msec)

Fig. 9

#81X0938

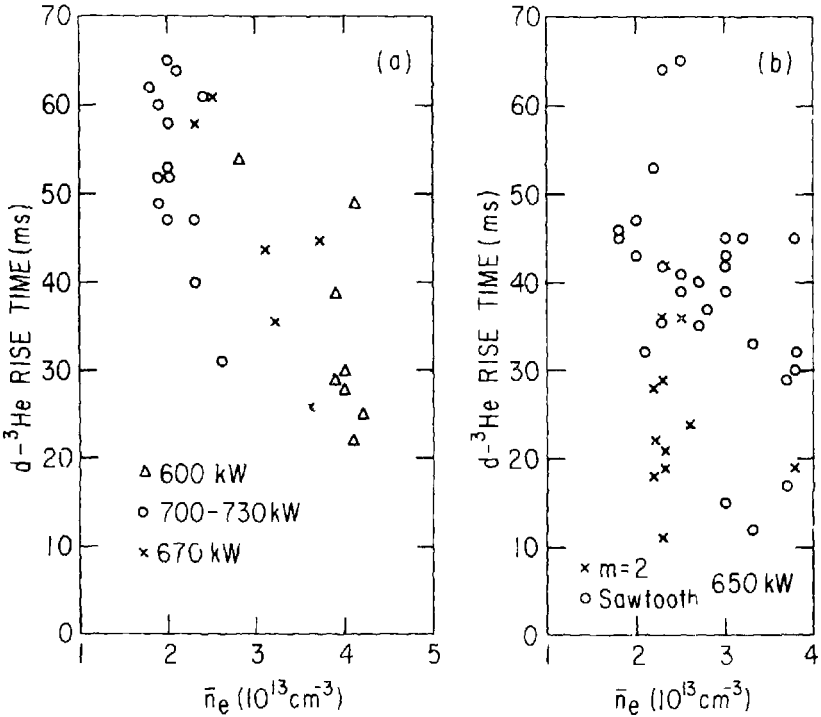

Fig. 10

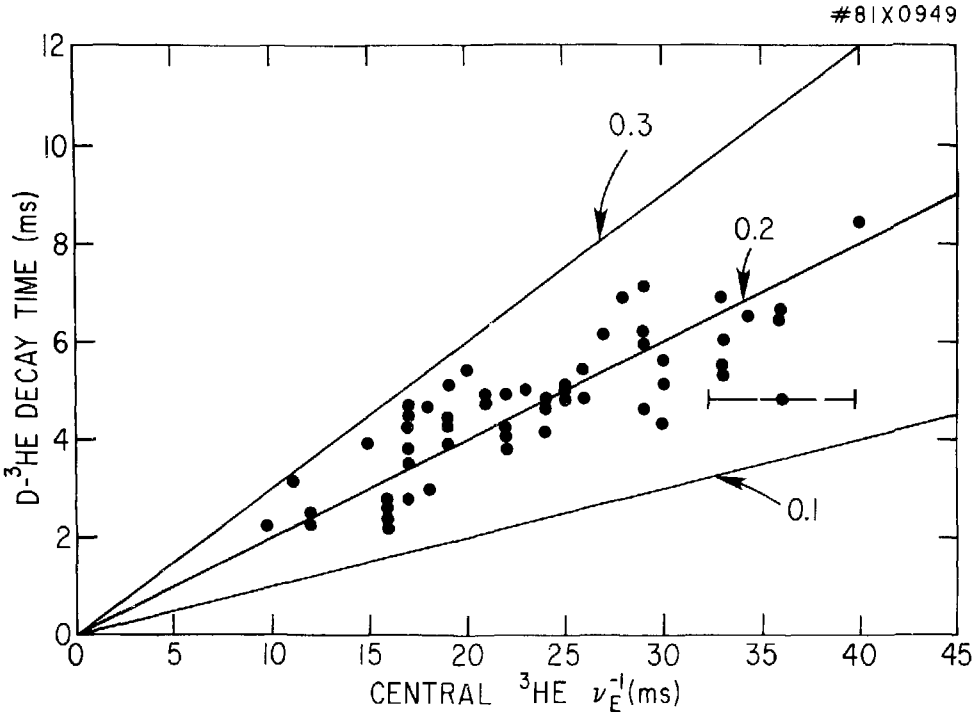
#81X0949
D-3HE DECAY TIME (ms)
CENTRAL 3HE ν_E^{-1}(ms)
0.3
0.2
0.1
0
2
4
6
8
10
12
0
5
10
15
20
25
30
35
40
45

Fig. 11

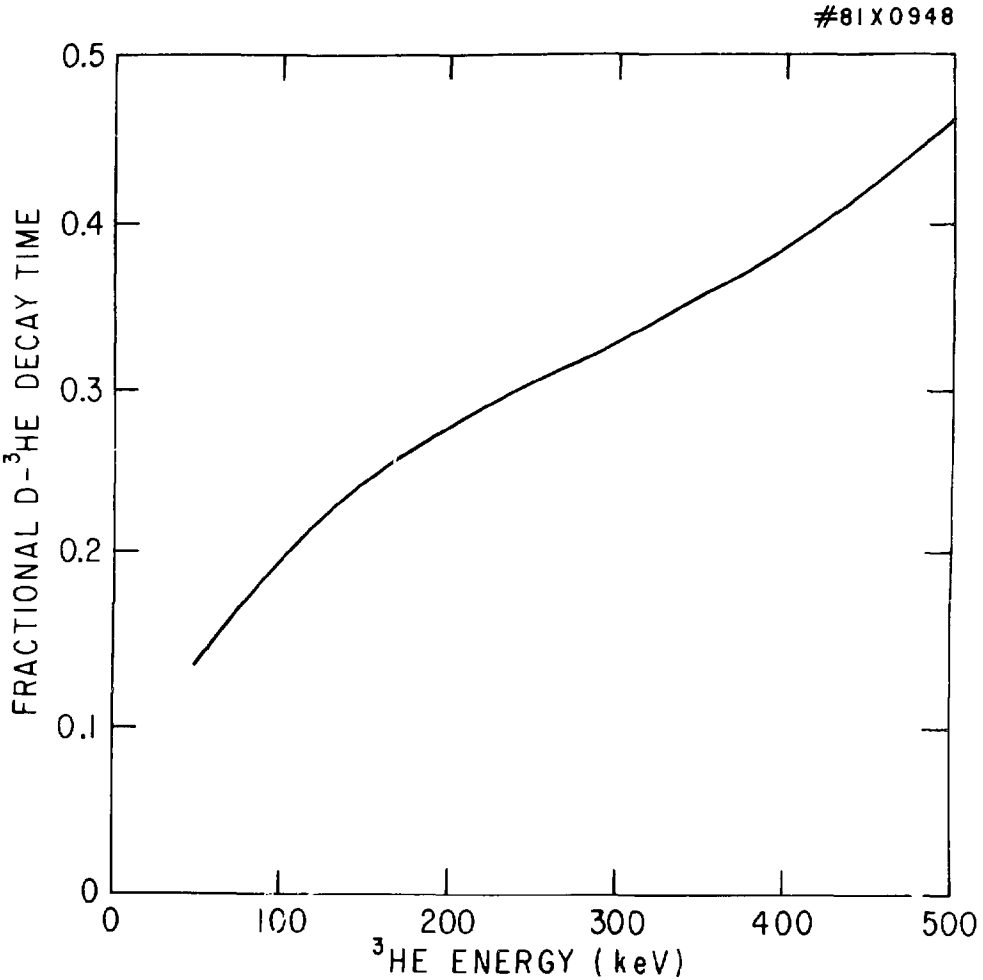
#81X0948
0.5
0.4
0.3
0.2
0.1
0
FRACTIONAL D-^{3}HE DECAY TIME
0
100
200
300
400
500
^{3}HE ENERGY (keV)

Fig. 12

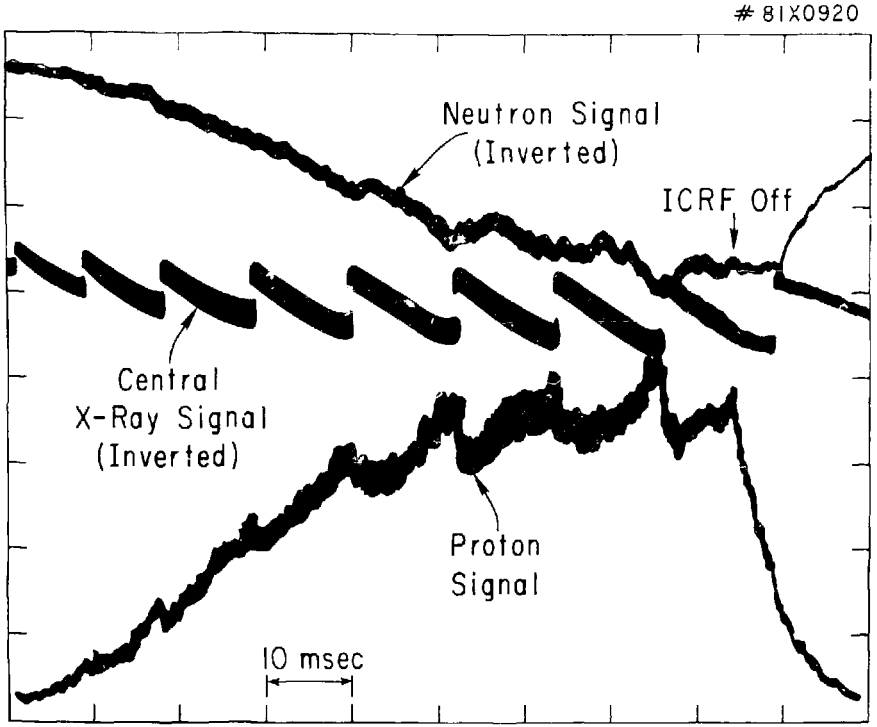
#81X0920
Neutron Signal
(Inverted)
ICRF Off
Central
X-Ray Signal
(Inverted)
Proton
Signal
10 msec

Fig. 13

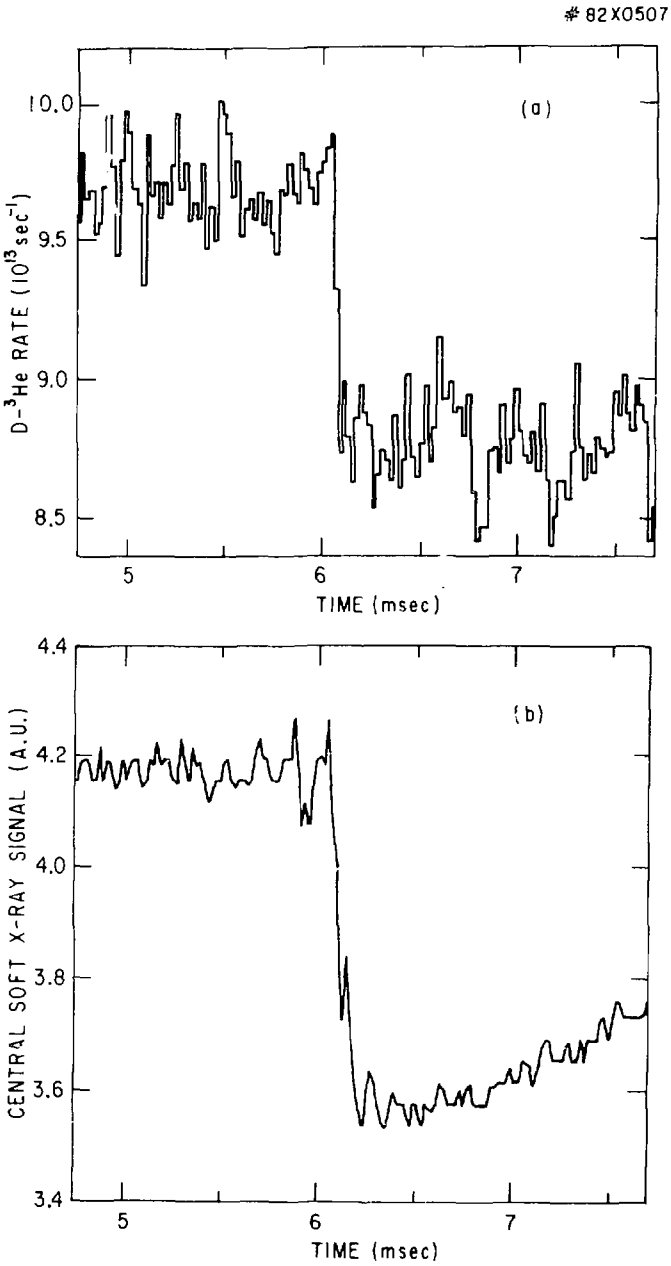
#82X0507
(a)
10.0
9.5
9.0
8.5
D-3He RATE (10^13 sec^-1)
5
6
7
TIME (msec)
(b)
4.4
4.2
4.0
3.8
3.6
3.4
CENTRAL SOFT X-RAY SIGNAL (A.U.)
5
6
7
TIME (msec)

Fig. 14

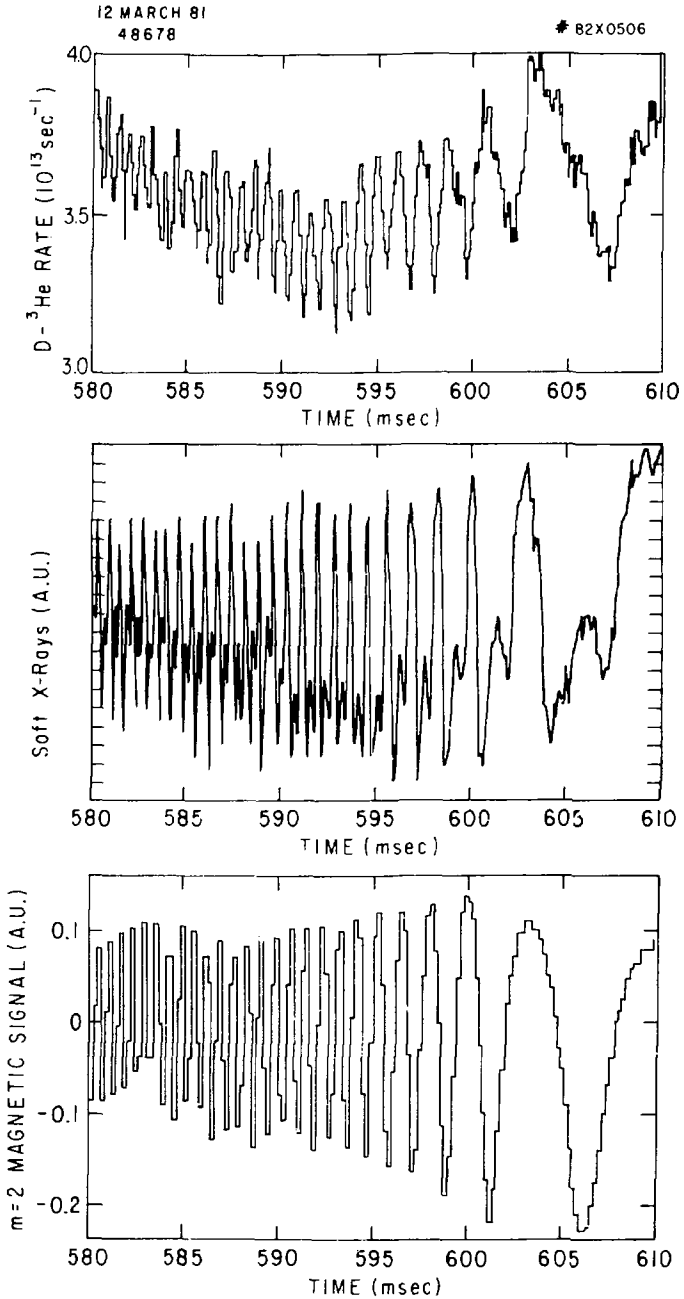
12 MARCH 81
48678
* 82X0506
D-^{3}He RATE (10^{13}sec^{-1})
4.0
3.5
3.0
580
585
590
595
600
605
610
TIME (msec)
Soft X-Rays (A.U.)
TIME (msec)
m=2 MAGNETIC SIGNAL (A.U.)
0.1
0
-0.1
-0.2
TIME (msec)

Fig. 15